Check for updates

Chemistry
Europe

European Chemical
Societies Publishing

Singlet Oxygen Oxidation of the Radical Cations of 8-Oxo-2′-deoxyguanosine and Its 9-Methyl Analogue: Dynamics, Potential Energy Surface, and Products Mediated by C5-O$_2$-Addition

May Myat Moe,[a, b] Midas Tsai,[c] and Jianbo Liu*[a, b]

8-Oxo-2′-deoxyguanosine (OG) is the most common DNA lesion. Notably, OG becomes more susceptible to oxidative damage than the undamaged nucleoside, forming mutagenic products in vivo. Herein the reactions of singlet O$_2$ with the radical cations of 8-oxo-2′-deoxyguanosine (OG$^{•+}$) and 9-methyl-8-oxoguanine (9MOG$^{•+}$) were investigated using ion-molecule scattering mass spectrometry, from which barrierless, exothermic O$_2$-addition products were detected for both reaction systems. Corroborated by static reaction potential energy surface constructed using multi-reference CASPT2 theory and molecular dynamics simulated in the presence of the reactants′ kinetic and internal energies, the C5-terminal O$_2$-addition was pinpointed as the most probable reaction pathway. By elucidating the reaction mechanism, kinetics and dynamics, and reaction products and energetics, this work constitutes the first report unraveling the synergetic damage of OG by ionizing radiation and singlet O$_2$.

Introduction

8-oxo-2′-deoxyguanosine (abbreviated as OG, the oxidized form of 2′-deoxyguanosine) is the most common DNA lesion[1] and used as a biomarker of oxidative stress induced by ionizing radiation, reactive oxygen species, chemical oxidation, photo-oxidation, etc. in cells and tissues.[2] The formation of OG and its secondary damage alter base pairing and stacking and affect the fidelity of transcription and replication,[3] which leads to mutagenesis, carcinogenesis and apoptosis. Particularly, OG participates in the G·C→T·A transversion mutation introduced by OG·A mispairing,[4] the DNA-protein cross linking,[5] and the neurological disorders associated with Alzheimer′s[6] and Parkinson′s diseases.[7] Besides the biological sequelae in aging and diseases, OG is implicated in photodynamic therapy,[8] wherein electronically excited singlet O$_2$ ([a$^1\Delta_g$])[9] is deliberately generated in the presence of light and a photosensitizer, followed by ^{1}O$_2$-induced destruction of cancerous and precancerous cells. The ^{1}O$_2$ damage to DNA targets exclusively guanine residues, producing OG in cellular DNA.[10]

OG is even more susceptible to ^{1}O$_2$, hydroxyl radicals and one-electron oxidants than guanosine,[10–11] and the oxidation products are more mutagenic in vivo than OG.[11k,12] Scheme 1 provides a summary of the ^{1}O$_2$ oxidation pathways and products of OG reported in literature.[3b,11a–c,11e–h,11j,11l,11n,11o,13] The reaction is initiated by a [2+2] addition of ^{1}O$_2$ across the 4,5-ethylenic bond, forming a 4,5-dioxetane. 4,5-dioxetane was detected only at temperature down to −80 °C and decomposed upon warming.[11a] It may produce a transient 9-membered macrocycle via 1,2-cleavage.[11a,c] The latter, upon ring closure with extrusion of CO$_2$, first rearranges to a 1,3,5-triazine-1(2H)-carboximidamide, 3-(2′-deoxy-β-D-erythro-pentofuranosyl) tetrahydro-2,4,6-trioxo, and then to a stable cyanuric acid nucleoside (Cya) and urea.[11a,c] An alternative decomposition pathway of 4,5-dioxetane starts with the opening of the dioxetane to form a hydroperoxide 5-OOH—OG.[11j] 5-OOH—OG decomposes to a complex array of products, of which the reduced hydroxyl product 5-OH—OG was relatively stable at −40 °C.[11a,j] The downstream conversion of 5-OH—OG is pH dependent.[11n,13b] Under acidic condition, formation of a protonated guanidinohydantoin [Gh+H]$^+$ via sequential hydrolysis, ring opening, decarboxylation and intramolecular hydrogen transfer is predominant. Under neutral and basic conditions, 5-OH—OG rearranges via an acyl shift to a spiroiminodihydantion [Sp − H]$^-$.[11h,j,n,13a] 5-OOH—OG may also undergo 5,6-bond cleavage and then decarboxylation to a dehydro-guanidinohydantoin (Gh^{ox}). The latter may evolve to 2-amino-5-((2′-deoxy-β-D-erytho-pentofuranosyl)amino)-4H-imidazole-4-one (Iz) and 2,2-diamino-4-((2′-deoxy-β-D-erytho-pentofuranosyl)amino)-5(2H)-oxazolone (Oz)[11b,h] as well as its ring-opened isomer guanidinooxalamide.[3b,11e,l]
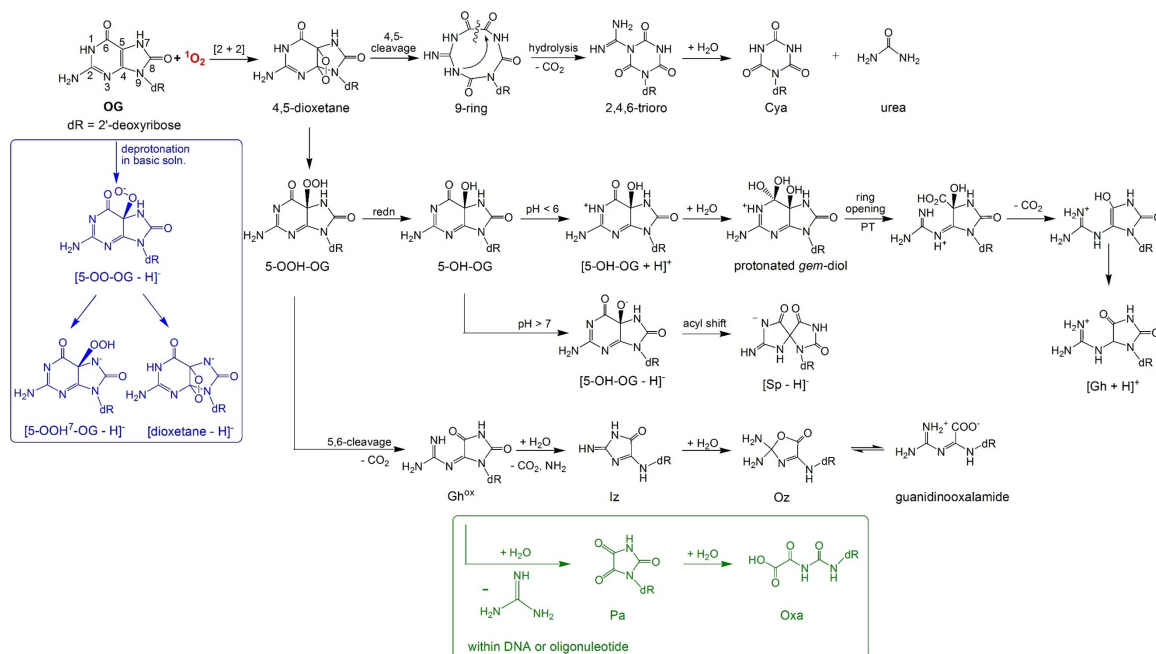
Note that the OG oxidation behavior depends on chemical contexts and reaction conditions. The oxidation of OG within DNA differs from that of an isolated monomer in that the Gh^{ox}

[a] M. M. Moe, Prof. Dr. J. Liu
Department of Chemistry and Biochemistry
Queens College of the City University of New York
65-30 Kissena Blvd., Queens, NY 11367 (USA)
E-mail: jianbo.liu@qc.cuny.edu
[b] M. M. Moe, Prof. Dr. J. Liu
Ph.D. Program in Chemistry
The Graduate Center of the City University of New York
365 5th Ave., New York, NY 10016 (USA)
[c] Prof. Dr. M. Tsai
Department of Natural Sciences
LaGuardia Community College
31-10 Thomson Ave., Long Island City, NY 11101 (USA)

ChemPlusChem

Full Papers
doi.org/10.1002/cplu.202100238

Chemistry Europe
European Chemical
Societies Publishing

Scheme 1. The $^1O_2$-oxidation pathways and products of 8-oxo-2′-deoxyguanosine.

intermediate contained in oligonucleotide undergoes hydration at the N3–C4 double bond (as shown in the green-colored structures in the Scheme), leading to parabanic acid (Pa) after release of guanidine and to oxaluric acid-containing oligonucleotide (Oxa) after further hydrolysis.[11f–h] We have also reported before that the oxidation of protonated 8-oxoguanine completely shuts down, whereas the oxidation of deprotonated 8-oxoguanine appears to be both energetically feasible and kinetically favorable (as shown in blue-colored structure in the Scheme).[11o] All of these findings have demonstrated the reaction diversities of OG and its nucleobase toward $^1O_2$ and warrant efforts to delineate reaction mechanisms at various oxidation scenarios.

Compared to the normal DNA nucleosides, OG has a much lower oxidation potential, *i.e.*, $E°$ *vs.* NHE is 0.58 V for OG,[14] 1.29 V for guanosine, 1.42 V for adenosine (A), 1.6 V for deoxycytidine (C), and 1.7 V for thymidine (T).[15] The same trend occurs in the adiabatic ionization energies (AIE) of nucleobases, *i.e.*, AIE = 6.38 eV for 8-oxoguanine,[16] 7.75 eV for guanine,[17] 8.27 eV for adenine, 8.66 eV for cytosine, and 8.82 eV for thymine.[18] Hence, OG acts as a deep trap for charge by forming OG$^{•+}$ radical cation upon ionizing radiation and one-electron oxidation,[11e,19] and the OG-containing DNA becomes more easily oxidizable.[20] A biologically significant scenario is ionizing radiation and $^1O_2$ interacting simultaneously with nucleic acids, wherein synergetic damage is anticipated from the combination of OG formation, conversion to OG$^{•+}$ and reaction with $^1O_2$. The study of these simultaneously occurring processes is important in understanding the oxidatively generated DNA damage and the synergetic effects in combining radiotherapy and photodynamic therapy for cancer treatment.[21] Surprisingly, to our knowledge, the reaction of OG$^{•+}$ with $^1O_2$ has not yet been

examined. This has motivated us to investigate the $^1O_2$ oxidation of OG$^{•+}$ and its model compound 9-methyl-8-oxoguanine (9MOG$^{•+}$) in the present work.

A complication of OG$^{•+}$ is that it becomes more acidic than its neutral molecule, *i.e.*, pK_{a1} = 8.6 for OG[22] *vs.* pK_{a1} = 6.6 for OG$^{•+}$.[23] This indicates that 72% of OG$^{•+}$ is deprotonated (at N7) and forms [OG − H]$^•$ in a neutral solution. However, within double-stranded (*ds-*) DNA, the N7–H of OG$^{•+}$ could be stabilized through the Hoogsteen mispairing with A, T, G or C (wherein the N7–H of OG$^{•+}$ is shared via a hydrogen bond with the N1 atom of A, the O2 atom of T, the O6 atom of G and the N3 atom of C, respectively).[24] A similar scenario was found for the guanosine radical cation (G$^{•+}$) within *ds-*DNA where G$^{•+}$ is stabilized through the Watson-Crick base pairing with C and diminishes the N1–H deprotonation.[25] Thus, a direct measurement of the $^1O_2$ reactions with G$^{•+}$ and OG$^{•+}$ in solution is not viable, as the primary radical cations undergo deprotonation faster[26] than oxidation, and [G − H]$^•$ and [OG − H]$^•$ follow different transformations and produce different products than their parent radical cations within *ds-*DNA.[27] For this reason, a rarefied gas-phase environment was utilized in this work for probing the chemistry of OG$^{•+}$, wherein the reactions were not perturbed by deprotonation and the system was examined by sensitive gas-phase techniques.[28] By capitalizing on mass spectrometric measurement of gas-phase ion-molecule collisions, augmented by direct dynamics simulations and reaction potential energy surface (PES) modeling, we have unraveled the intrinsic reaction mechanism, reaction kinetics and thermodynamics of OG$^{•+}$ with $^1O_2$.

ChemPlusChem

Full Papers
doi.org/10.1002/cplu.202100238

**Chemistry
Europe**
European Chemical
Societies Publishing

Results and Discussion

Formation and structures of 9MOG•+ and OG•+

Nucleobase and nucleoside radical cations may be generated in the gas phase by photoionization,[17–18] electron-impact ionization[29] and fast atom bombardment,[30] but the processes are accompanied by fragmentation and internal excitation. Siu and coworkers discovered that collision-induced electron transfer in doubly charged ternary Cu[II] complex could produce radical cations of oligopeptide in the gas phase.[31] The O'Hair[28a,b,32] and Bohme[28c] laboratories extended this approach to the formation of guanosine radical cations via collision-induced dissociation (CID) of Cu(II)-nucleoside(G) complexes wherein the redox separation of $[Cu^{II}G_3]^{•2+}$ leads to the formation of complementary product ions $G^{•+}$ and $[Cu^I G_2]^+$. This method was successfully used to generate the radical cations of guanine, 9-methylguanine, 2'-deoxyguanosine and guanosine,[28h,33] as well as those of Hachimoji nucleobases.[28e–g]

In the present work, 9MOG•+ was generated by CID of the $[Cu^{II}(9MOG)_{3-n}(2'\text{-deoxyguanosine})_n]^{•2+}$ ($n=0$–2) complexes which were formed by electrospray ionization (ESI) of a methanol/water solution containing equimolar concentration of 9MOG, 2'-deoxyguanosine (used as a co-ligand) and $Cu(NO_3)_2$. Similarly, OG•+ was generated by CID of $[Cu^{II}(OG)_{3-n}(2'\text{-deoxyguanosine})_n]^{•2+}$.

9MOG and OG have numerous tautomers/rotamers formed by keto-enol tautomerization, amino-imino tautomerization, proton migration and the rotation of side group, of which the 6,8-diketone structure is the predominant one while 6-enol-8-ketone is the second important.[11n,11o,34] Like their neutral molecules, both 9MOG•+ and OG•+ adopt the 6,8-diketone structure as their global minimum energy conformations.[11n] The 6-enol-8-keto structures of 9MOG•+ and OG•+ each have two conformations, one is formed by the keto-enol isomerization of N1H–O6 (i.e., anti-6-enol-8-ketone) and the other by the keto-enol isomerization of N7H–O6 (i.e., syn-6-enol-8-ketone). As exemplified by the 9MOG•+ conformers in Figure S1 (Supporting Information), anti- and syn-6-enol-8-ketone lie at energy 0.17 and 0.81 eV higher than 6,8-diketone, respectively, rendering their contributions negligible.

Scheme 2 plots spin densities, charge distributions and singly occupied molecular orbitals (SOMOs) of 9MOG•+ and OG•+. In both structures, the unpaired electron and SOMO are delocalized mostly among the C2, N3, C4, C5 and N7 sites, with some spreading around the N2, O6, C8–O8 and N9 sites. The oxidized imidazole ring is more positively charged ($\delta^+ = 0.82$–0.86 including the N9-group) than the 6-membered ring ($\delta^+ = 0.5$–0.6), and the C8 position is the most positively charged atom ($\delta^+ = 0.74$). The only difference between 9MOG•+ and OG•+ is that the negative charges at the N3, O8 and N9 atoms decreases from −0.47, −0.41 and −0.21 in 9MOG•+ to −0.41, −0.39 and −0.17 in OG•+, respectively, whereas the positive charge at the C5 position decreases from 0.45 in 9MOG•+ to 0.33 in OG•+.

spin and charge

SOMO

9MOG•+   OG•+
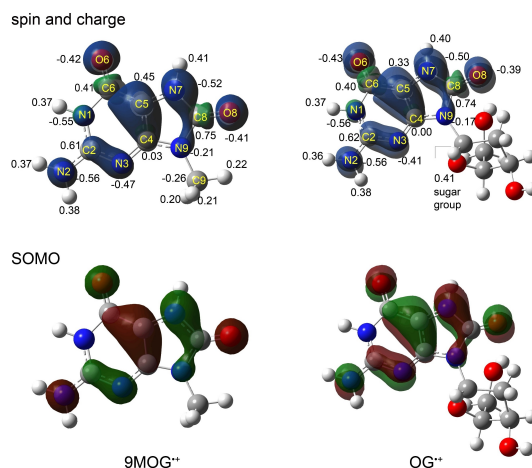
Scheme 2. Global minimum energy structures of 9MOG•+ and OG•+, with atom numbering schemes. Geometries, spin densities (represented by contour plots) and atomic charges (indicated in numbers) were calculated at ωB97XD/6-31 + G(d,p), and SOMOs were evaluated at CASSCF(9,7)/6-31 + G(d,p). Their Cartesian coordinates are available in the Supporting Information.

Oxidation products, cross sections and reaction efficiencies of 9MOG•+ and OG•+

We have measured the reactions of $^1O_2$ with 9MOG•+ and OG•+ in the gas phase, each over the center-of-mass collision energy (E_{col}) range of 0.05–1.0 eV. The experiment was conducted on a home-built guided-ion beam tandem mass spectrometer coupled with an ESI ion source.[35] The $^1O_2$-oxidation products of 9MOG•+ (m/z 181) and OG•+ (m/z 283) were observed at m/z 213 and 315, respectively, which correspond to the formation of respective O_2-adducts. The product cross sections ($\sigma_{reaction}$) are shown in Figure 1 as a function of E_{col}, in which error bars were determined from 4 sets of measurements. Representative product ion mass spectra are presented in the inset of the figure. For both reaction systems, product cross sections increase with decreasing E_{col}, indicating that these product channels are exothermic and have no reaction activation barriers located above the reactants.

A closer examination of the radical ion reactivity with $^1O_2$ was done by evaluating its reaction efficiency. The reaction efficiencies were calculated by $\sigma_{reaction}/\sigma_{collision}$, where $\sigma_{collision}$ represents the ion-induced dipole capture cross section.[36] The results were represented by dark-green lines in Figure 1. The $^1O_2$-oxidation efficiency of 9MOG•+ has maintained at 2.3–2.6% at the E_{col} range from 0.05 to 0.15 eV, decreased to 2.0% at 0.2 eV, 1.5% at 0.25 eV and 1.2% at 0.3 eV, and became negligible at energies above 0.5 eV. Such E_{col} dependence implies that the reaction is mediated by a complex, but the complex formation and lifetime are strongly inhibited by collision energy. Compared to that of 9MOG•+ at the same E_{col}, the reaction efficiency of OG•+ decreases by nearly half, being 0.9–1.3% at $E_{col} = 0.05$–0.15 eV, dropping to 0.7% at 0.2 eV, 0.6% at 0.25 eV, and ≤ 0.5% at $E_{col} \geq 0.3$ eV. The relatively lower reaction efficiency of OG•+ might be attributed to the quenching of $^1O_2$ by its sugar group. A similar extent of reaction
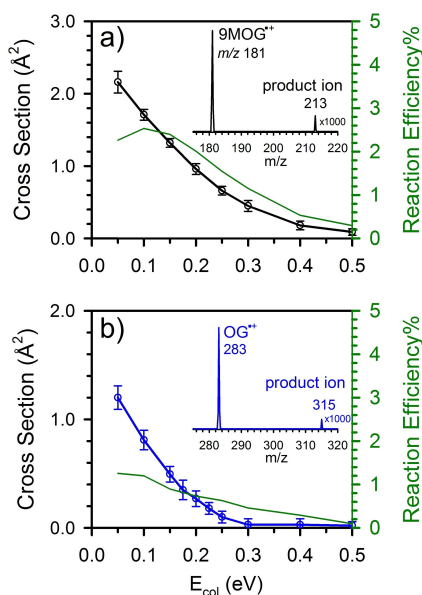
Figure 1. Product cross sections and reaction efficiencies (right axis) for the $^1O_2$ reactions with (a) 9MOG$^{\bullet+}$ and (b) OG$^{\bullet+}$, wherein vertical bars denote uncertainties. Insets show product ion mass spectra obtained at $E_{col} = 0.05$ eV, where the product ion intensity were scaled by a factor of 1000.

inhibition by the sugar group was observed in the $^1O_2$ reactions with the radical cations of 2′-deoxyguanosine and guanosine,[28h] where the efficiencies of the two nucleosides are only half compared to the radical cations of guanine and 9-methylguanine, albeit that all of the reactant ions presented the same E_{col} dependence.

According to our recent work,[28h] the maximum $^1O_2$ reaction efficiencies with the radical cations of 9-methylguanine and 2′-deoxyguanosine are 1.4% and 0.7%, respectively (both were

observed at $E_{col} = 0.05-0.1$ eV). Therefore, the $^1O_2$ oxidation efficiencies of 9MOG$^{\bullet+}$ and OG$^{\bullet+}$ are a factor of two higher than those of the radical cations of 9-methylguanine and 2′-deoxyguanosine. As mentioned earlier, 8-oxoguanine and OG are more reactive toward $^1O_2$ than their parent nucleobase and nucleoside. The present experiment indicates that the same trend exists in their ionized radical cations.

$^1O_2$-addition pathways predicted by density functional theory (DFT) and molecular dynamics

The experiment has confirmed that 9MOG$^{\bullet+}$ and OG$^{\bullet+}$ produced similar products and E_{col} dependence with $^1O_2$. The previous computational analyses have also indicated that the N9-substitution (such as H, CH$_3$, CH$_2$OH, CH(CH$_3$)OCH$_3$ in place of the sugar) of guanosine[37] and OG[38] does not affect their $^1O_2$-oxidation mechanisms and energetics. These suggest that 9MOG$^{\bullet+}$ should provide a good prototype for simulating OG$^{\bullet+}$ reactions. We have first constructed the static reaction coordinates for 9MG$^{\bullet+}$ with $^1O_2$ at the ωB97XD/6-31 + G(d,p) level of theory. The long-range corrected hybrid density functional ωB97XD[39] was chosen to mitigate self-interaction errors and improve the radical orbital description.[40]

As shown in Scheme 3, the reaction of 9MOG$^{\bullet+}$ + $^1O_2$ is initiated at a reactant-like, π-stacked precursor complex formed through a barrierless, exothermic process. All possible pathways that may evolve from the precursor complex were considered in the calculations, including those that are endothermic and/or bear high activation barriers and thus may not occur in the experimental E_{col} range of 0.05–1.0 eV. Four distinctively different $^1O_2$-addition pathways have been inferred from the DFT calculations, each of which is discussed below. For each pathway, reaction intermediates and products are presented in GaussView structures together with their formation enthalpies
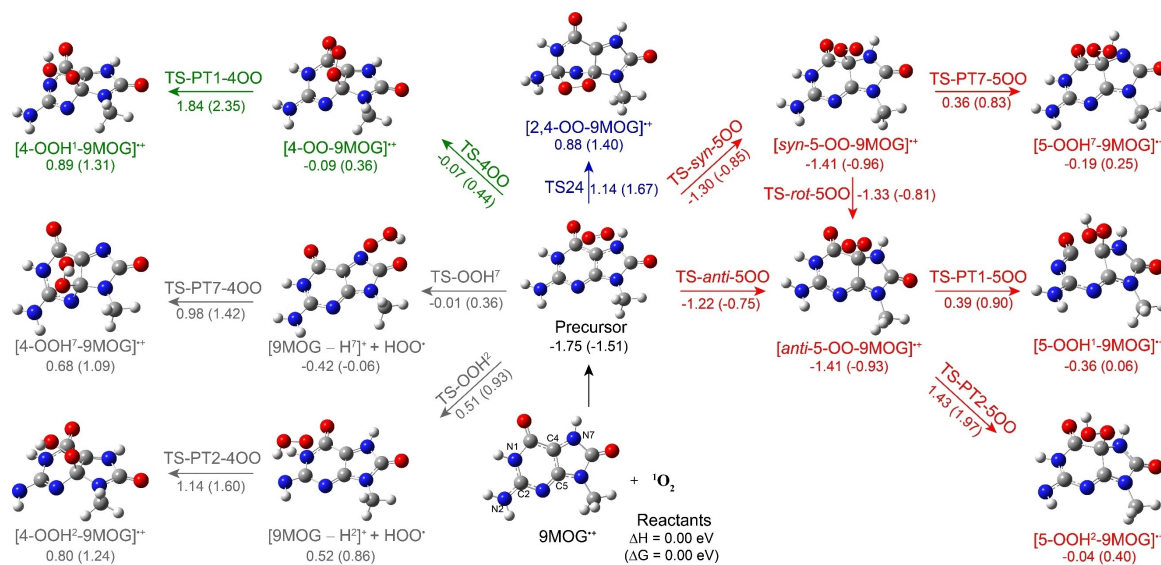
Scheme 3. Reaction pathways for 9MOG$^{\bullet+}$ with $^1O_2$. Reaction enthalpies and Gibbs free energy (in parentheses) were calculated at ωB97XD/6-31 + G(d,p), including thermal corrections at 298 K. Cartesian coordinates of reaction structures are available in the Supporting Information.

ChemPlusChem

Full Papers
doi.org/10.1002/cplu.202100238

**Chemistry
Europe**
European Chemical
Societies Publishing

(ΔH), Gibbs free energies (ΔG, indicated in parentheses) and activation energies with respect to the reactants at 298 K.

1) Concerted cycloaddition of $^1O_2$ (which acts as a dienophile) across the C2–C4 bond of 9MOG$^{\bullet+}$. The pathway (labelled in blue in Scheme 3) is mediated by TS24 and leads to the formation of a [2,4-OO–9MOG]$^{\bullet+}$ endoperoxide. As the O_2 moiety is electron deficient, the positive charge retains at the oxidized imidazole ring throughout the reaction. The unpaired electron, on the other hand, shifts from 9MOG to O_2 in the precursor complex (i.e., form a distonic radical cation[41]), and then diffuses over the whole structure in TS24 and [2,4-OO–9MOG]$^{\bullet+}$. As 9MOG$^{\bullet+}$ adopts a 6,8-diketone structure and thus lacks a N7–C8 double bond, a [4+2] cycloaddition to the 5-membered ring can be excluded. Moreover, unlike the protonated and deprotonated 8-oxoguanine which may form a 2,5-endoperoxide and/or a 4,5-dioxetane,[11o] neither of the 2,5- and 4,5-addition is feasible for 9MOG$^{\bullet+}$.

2) C4-terminal addition of O_2 (labelled in green). The addition produces a [4-OO–9MOG]$^{\bullet+}$ peroxide via TS-4OO, wherein the O_2 moiety is oriented in parallel with the C4–C5 bond. [4-OO–9MOG]$^{\bullet+}$ may serve as an intermediate for proton transfer from N1–H to the distal O atom of the peroxo group via TS-PT1-4OO, yielding a hydroperoxide [4-OOH^1–9MOG]$^{\bullet+}$ (the superscript indicates the origin of the transferred proton). The unpaired electron remains at the O_2 moiety in TS-4OO and [4-OO–9MOG]$^{\bullet+}$, but diffuses to the 9MOG moiety along the proton transfer pathway.

We have tried to locate reaction pathways leading to [4-OOH^2–9MOG]$^{\bullet+}$ and [4-OOH^7–9MOG]$^{\bullet+}$ hydroperoxides by transferring a N2–H or N7–H to the peroxo group in [4-OO–9MOG]$^{\bullet+}$, but no connecting transition states (TSs) could be identified. As described in pathway 4, these two hydroperoxides are formed by convoluted mechanisms.

3) C5-terminal addition of O_2 (labelled in red). There are two routes, both of which lead to a 5-OO-peroxide but with syn- and anti-conformations regard to the oxidized imidazole ring, i.e. syn-[5-OO–9MOG]$^{\bullet+}$ and anti-[5-OO–9MOG]$^{\bullet+}$. $^1O_2$ attacks the C5 via TS-syn-5OO to produce syn-[5-OO–9MOG]$^{\bullet+}$. In another route, anti-[5-OO–9MOG]$^{\bullet+}$ forms from the reactants by crossing over TS-anti-5OO. The two rotamers have similar activation barriers for formation and the identical formation exothermicity. They interconvert via a small rotation barrier TS-rot-5OO. Both [5-OO–9MOG]$^{\bullet+}$ peroxides present a prominent distonic character consisting of the O_2-centered spin and the 9MOG-centered positive charge. The formation of [5-OO–9MOG]$^{\bullet+}$ appears to be more kinetically feasible (with lower activation barriers) and energetically favorable (with higher exothermicities) than that of [4-OO–9MOG]$^{\bullet+}$, presumably because the C5-position presents a higher spin density for electrophilic addition.

Syn- and anti-[5-OO–9MOG]$^{\bullet+}$ may each have proton transfer to the end of the peroxo group. The proton transfer from N7–H in syn-[5-OO–9MOG]$^{\bullet+}$ via TS-PT7-5OO yields a [5-OOH^7–9MOG]$^{\bullet+}$ hydroperoxide, while that from N1–H and N2–H in anti-[5-OO–9MOG]$^{\bullet+}$ yield [5-OOH^1–9MOG]$^{\bullet+}$ and [5-OOH^2–9MOG]$^{\bullet+}$, respectively. Note that, although we have adopted the 9MOG atom numbering for [5-OOH^1–9MOG]$^{\bullet+}$, the

C5–C6 bond therein is ruptured (the bond length increases to 1.76 Å).

4) Hydrogen atom abstraction (HA, labelled in gray). The last pathway corresponds to the abstraction of a H atom in 9MOG$^{\bullet+}$ by $^1O_2$, followed by re-combination of dehydrogenated [9MOG − H]$^+$ cation and HOO$^\bullet$ to 4-hydroperoxides, i.e., precursor→TS-OOH7→[9MOG − H^7]$^+$ + HOO$^\bullet$→TS-PT7-4OO→[4-OOH^7–9MOG]$^{\bullet+}$ and precursor→TS-OOH2→[9MOG − H^2]$^+$ + HOO$^\bullet$→TS-PT2-4OO→[4-OOH^2–9MOG]$^{\bullet+}$. A general finding is that the hydroperoxides (including [4-OOH^1–9MOG]$^{\bullet+}$, [4-OOH^2–9MOG]$^{\bullet+}$, [4-OOH^7–9MOG]$^{\bullet+}$, [5-OOH^1–9MOG]$^{\bullet+}$, [5-OOH^2–9MOG]$^{\bullet+}$ and [5-OOH^7–9MOG]$^{\bullet+}$) require higher activation energies and/or large formation endothermicities than their parent peroxides.

In addition to static reaction coordinate calculations, we have simulated the collision dynamics of 9MOG$^{\bullet+}$ with $^1O_2$ using the direct dynamics approach.[42] The Venus program[43] was used to mimic the initial reactant rotational and vibrational energies and the random orientations of the collision partners. The Hessian-based predictor-corrector algorithm[42f] implemented in Gaussian 09[44] was used to integrate trajectories. The ωB97XD/6-31G(d) level of theory was selected for trajectory integration on the basis of its best accuracy/cost ratio. A batch of 150 trajectories was accumulated for 9MOG$^{\bullet+}$ + $^1O_2$ at E_{col} = 0.05 eV. The trajectory results show that $34\pm4\%$ of the ion-molecule collisions formed a precursor complex. The remaining $66\pm4\%$ belong to direct non-reactive collisions, with the collision time ($\tau_{collision}$, characterized as a length of time during which the two reactants approach within 5.0 Å of the center-of-mass (CM) distance) is less than 400 fsec. This time is comparable to the direct "fly by" time for a 5.0 Å CM distance.

Among the precursor complexes formed in the trajectories, $33\pm6\%$ (i.e., 17 trajectories) has initiated the $^1O_2$ attack toward the C5 position and $6\pm3\%$ (i.e., 3 trajectories) toward the C4 position. The branching ratio of C5- vs. C4- attack agrees with the DFT-calculated reaction thermodynamics and kinetics. Figure 2 demonstrates the most probable trajectory reaction which forms [5-OO–9MOG]$^{\bullet+}$ from a precursor complex. Figure 2a plots the change in the system potential energy (PE, left axis) and the CM distance (right axis) between 9MOG$^{\bullet+}$ and O_2. Oscillations in the PES reflect the reactant/product vibration. Figure 2b displays the changes in the two bond lengths rC5–OO and rO–O which are the most relevant to the reaction. In this trajectory, the formation of [5-OO–9MOG]$^{\bullet+}$ happened at 160 fsec (after the formation of the precursor complex), which is indicated by the abrupt shortening of rC5–OO to a covalent bond length. Figure 2c shows the interconversion of the syn- and anti-[5-OO–9MOG]$^{\bullet+}$ rotamers throughout the trajectory, as indicated by the change in the dihedral angle D(C4–C5–O–O). A positive D(C4–C5–O–O) represents a syn-rotamer whereas a negative one represents an anti-rotamer. The discontinuity of D(C4–C5–O–O) at the syn-to-anti conversion is artifact because the range of a dihedral angle is −180°– 180°. The conversion between the two rotamers does not obviously raise PE. This led us to expect that the isomerization was rather facile and resulted in an equilibrium composition of syn- and anti-[5-OO–9MOG]$^{\bullet+}$ in the product.

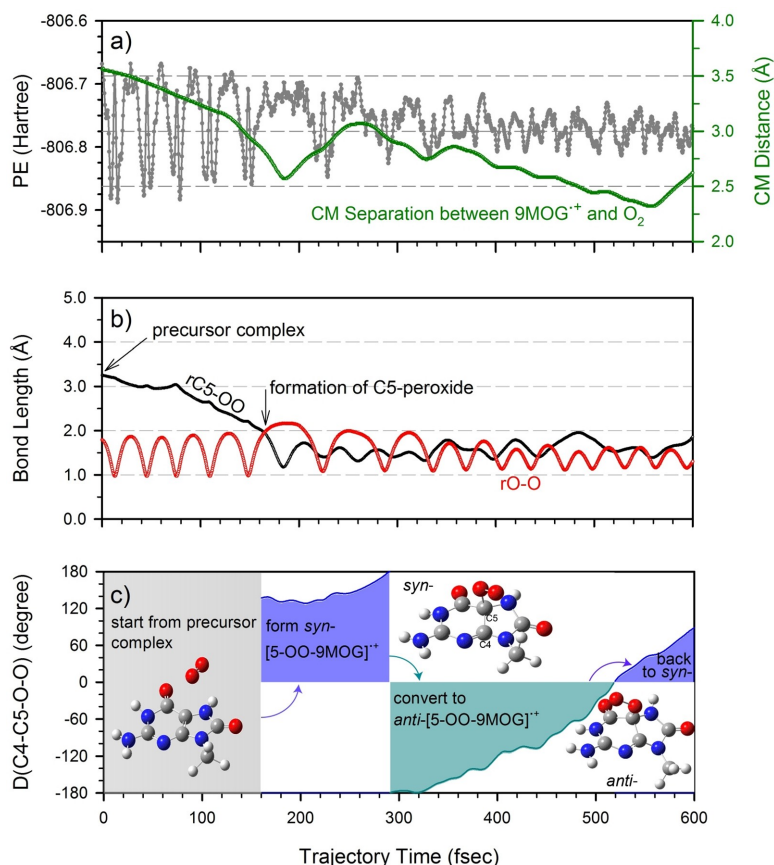**Figure 2.** A representative trajectory for the formation of [5-OO–9MOG]•+ from the collision of 9MOG•+ with ¹O₂ at $E_{col} = 0.05$ eV. (a) The variations in the potential energy (PE) and in the center-of-mass distance between the collision partners, (b) the changes of various bond lengths participating in the reaction, and (c) the interconversion between the *syn*- and *anti*-[5-OO–9MOG]•+, as indicated by the change of the C4–C5–O–O dihedral angle throughout the trajectory.

Reaction energies at DLPNO-CCSD(T) and T1 diagnostics of wavefunctions

Following the identification of probable reaction pathways and reaction coordinates, electronic energies of the ωB97XD-optimized stationary structures and TSs were calculated at the DLPNO-CCSD(T)/aug-cc-pVTZ level of theory, *i.e.*, the domain based local pair-natural orbital coupled-cluster single-, double- and perturbative triple-excitations method.[45] Table S1 (Supporting Information) compares reaction enthalpies calculated at ωB97XD/6-31+G(d,p) and DLPNO-CCSD(T)/aug-cc-pVTZ, respectively. Reactions PESs based on the two single-reference theories are presented in Figures S2 and S3 (Supporting Information). In both PESs, the C4- and C5-addition pathways are exothermic with no activation barriers above the reactants (except that the energy of TS-4OO is near thermal at DLPNO-CCSD(T)). [5-OO–9MOG]•+ appears to be more stable than its C4-analogue, and the *anti*- and *syn*-conformers of [5-OO–9MOG]•+ have the same formation enthalpy, with the *syn*-rotamer being slightly more kinetically favorable. However, large differences were observed between the reaction energies calculated at ωB97XD *vs.* DLPNO-CCSD(T). Particularly, the calculated energies of the precursor complex, TS24, TS-PT1-4OO, TS-PT7-5OO, [5-OOH¹–9MOG]•+ and TS-OOH⁷ strongly

depend on the theory. For these species, the DLPNO-CCSD(T) energies are at least 0.3 eV higher than the ωB97XD values, except for the precursor complex for which the energy increases by 1.14 eV at DLPNO-CCSD(T).

Note that, due to the mixed open- and closed-shell character of ¹O₂,[46] single Slater-determinant wavefunctions may not accurately describe the electronic structures of ¹O₂ and its reaction adducts.[28h] To verify whether the reaction structures are dominated by single-determinant wavefunctions, T1 diagnostic[47] was performed using DLPNO-CCSD(T)/aug-cc-pVTZ and the results are included in Table S1. Different than a closed-shell system for which a T1 diagnostic larger than 0.02 indicates an important multiconfigurational character,[47b,48] it is not clear what exactly constitutes a suspiciously large T1 for an open-shell system. But the T1 diagnostic has allowed us to vision how the multiconfigurational character evolves along individual pathways. A strong correlation was observed between T1 diagnostic and spin density distribution. Most of the reaction species that have shown large deviations between ωB97XD and DLPNO-CCSD(T) energies have the T1 exceeding 0.026, and these are the structures that delocalize the spin density on nucleobase and O₂.

We have also examined the values of $<S^2>$ before and after the annihilation of spin contamination in the unrestricted

ChemPlusChem

Full Papers
doi.org/10.1002/cplu.202100238

Chemistry
Europe
European Chemical
Societies Publishing

wavefunctions. The expected values of $<S^2>$ is 0.000 and 0.750 for pure singlet and doublet states, respectively. The structures, which have the large energy changes between ωB97XD and DLPNO-CCSD(T), all have the $<S^2>$ larger than the expected value. Especially, the precursor complex has $<S^2>=0.821$ even after the annihilation of spin contamination.

Reaction PES refined at CASSCF and CASPT2

In view of the deficiencies of DLPNO-CCSD(T), we have explored reaction PES at the complete active space self-consistent field level (i.e. CASSCF)[49] coupled with the 6-31+G(d,p) basis set. The active spaces are (9, 7) for 9MOG[•+], (12, 8) for $^1O_2$, and (21, 15) for the reaction structures, which include the $\sigma_{O(2s)-O(2s)}$, $\sigma^*_{O(2s)-O(2s)}$, $\sigma_{O(2p)-O(2p)}$, $\pi_{\pm 1}$, $\pi^*_{\pm 1}$ and $\sigma^*_{O(2p)-O(2p)}$ of O_2 and the π and σ_{N-H} orbitals of 9MOG[•+] that have participated in the formation of peroxides and hydroperoxides. The CASSCF reaction enthalpy was calculated on the basis of the electronic energy at CASSCF(21,15)/6-31+G(d,p) and the 298 K thermal correction at ωB97XD/6-31+G(d,p).

Figures 3–6 plot the CASSCF PES for 2,4-cycloaddition, C4- and C5-terminal addition and HA, respectively. The CASSCF reaction pathways follow the same reaction coordinates as those predicted by the single-reference theories, and the CASSCF-predicted SOMO orbitals are consistent with the ωB97XD-calculated spin density distributions. Nonetheless, the CASSCF calculations significantly increased reaction energies. Note that the CASSCF calculations included primarily non-dynamic electronic correlation. It is not unusual that CASSCF may have overestimated reaction energies and activation barrier heights, as revealed in the experimental and computational study of the $^1O_2$ oxidation of neutral guanine[50] and 9MG[•+].[28h]

To evaluate the effects of dynamic correlation and thus the accuracy of CASSCF results, we have adopted the CASPT2 method.[51] CASPT2 adds the dynamic correlation using second-order perturbation theory with the CASSCF wavefunction as the reference. It treats dynamic correlation effects perturbatively and thus is less expensive than the multi-reference configuration interaction method.[52] A composite CASPT2/DFT approach (i.e., single-point CASPT2 energy calculations of DFT-optimized geometries) was able to produce correct PESs for the $^1O_2$ reactions with alkenes,[46] 1,3-cyclohexadiene,[50,53] guanine[54] and histidine.[54] We have recently applied DFT, RI-MP2 (the resolution-of-the-identity second-order Møller-Plesset perturbation theory),[55] DLPNO-CCSD(T), CASSCF and CASPT2 in the PES calculation for the $^1O_2$ oxidation of 9MG[•+], of which the CASPT2 results yielded the best agreement with the experiment.[28h]

The performance of CASPT2 vs. CASSCF may be comprehended in Figures 3–6, wherein the energy differences between the two methods are indicated. It appears that dynamic correlations are the most significant in TS24 (−0.84 eV), TS-4OO (−1.19 eV), [4-OO–9MOG][•+] (−1.15 eV), TS-PT1-4OO (−1.67 eV), [4-OOH[1]–9MOG][•+] (−1.18 eV), TS-PT1-5OO (−2.02 eV), [5-OOH[1]–9MOG][•+] (−2.63 eV), TS-PT2-5OO (−2.85 eV), TS-OOH[2] (−1.15 eV), TS-PT2-4OO (−0.81 eV) and TS-PT7-4OO (−1.07 eV), where the numbers in the parentheses represent the energy corrections by CASPT2. The correction becomes less prominent (less than 0.5 eV) for syn- and anti-[5-OO–9MOG][•+] and for their formation and rotation TSs, all of which have T1 diagnostics not exceeding 0.02.

It is informative to compare CASPT2 with the single-reference results. For most of the reaction species, the ωB97XD energy is 0.5–0.7 eV lower than the CASPT2 energy. This energy difference matches the amount of excitation energy that was overestimated (0.7 eV) for $^1O_2$ by the spin restricted ωB97XD. The exceptions are for some TSs and HA products, of which the

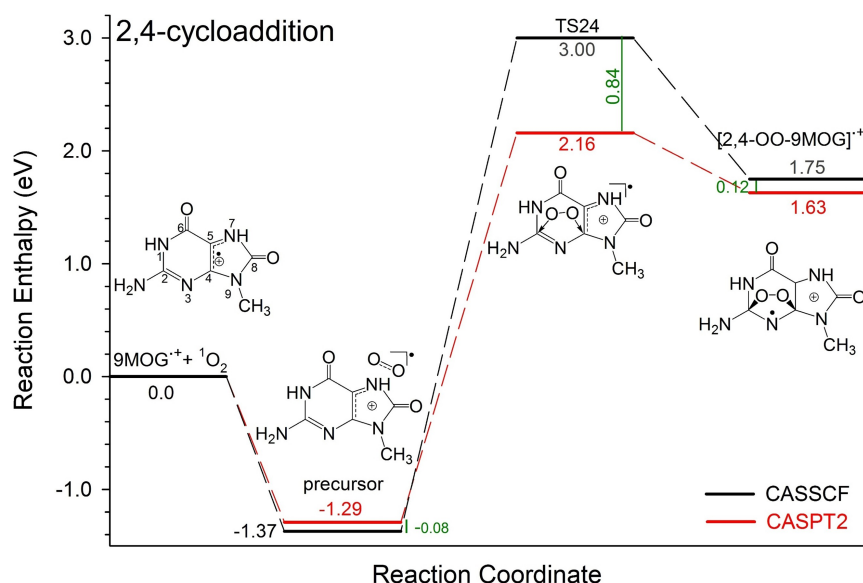**Figure 3.** Comparison of the PES for the 2,4-cycloaddition of $^1O_2$ to 9MG[•+] calculated at CASSCF(21, 15)/6-31+G(d,p) and CASPT2(21,15)/6-31G(d,p), using the ωB97XD/6-31+G(d,p)-optimized geometries. Reaction enthalpies were calculated at 298 K including thermal corrections. Reaction structures and rearrangements in TSs are shown in the ChemDraw scheme.

ChemPlusChem

Full Papers
doi.org/10.1002/cplu.202100238

Chemistry Europe
European Chemical
Societies Publishing

Figure 4. Comparison of the PES for the C4-addition of $^1O_2$ to 9MG$^{\bullet+}$ calculated at CASSCF(21,15)/6-31+G(d,p) and CASPT2(21,15)/6-31G(d,p), using the ωB97XD/6-31+G(d,p)-optimized geometries. Reaction enthalpies were calculated at 298 K including thermal corrections. Reaction structures and rearrangements in TSs are shown in the ChemDraw scheme.
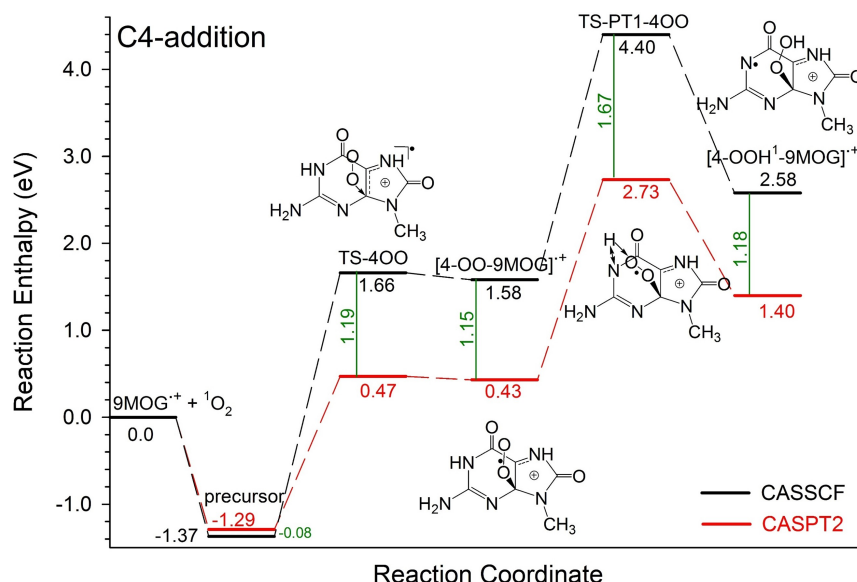
CASPT2 and ωB97XD energies differ either less than 0.5 eV (i.e., TS-syn-5OO, TS-anti-5OO, [5-OOH^1–9MOG]$^{\bullet+}$, TS-PT2-5OO, [9MOG − H^2]$^+$+HOO$^\bullet$ and [4-OOH^2–9MOG]$^{\bullet+}$) or more than 0.8 eV (i.e., TS24, TS-PT1-4OO and TS-PT7-5OO). Compared to CASPT2, DLPNO-CCSD(T) also overestimated the $^1O_2$ excitation energy by 0.4 eV whereas decreased most of the reaction energies by a range of 0.4–0.7 eV, except that the precursor complex became less stable by 0.68 eV at DLPNO-CCSD(T).

According to the CASPT2 PES, the most probable product channel corresponds to reactants→precursor→TS-syn-5OO/TS-anti-5OO→syn- and anti-[5-OO–9MOG]$^{\bullet+}$. Syn- and anti-[5-OO–9MOG]$^{\bullet+}$ have the same formation ΔH (i.e. −0.84 eV), and their activation barriers shift to an energy below the products. Therefore, the reactions are barrierless.

Comparison with the $^1O_2$ oxidation of protonated and deprotonated 8-oxoguanine

We have previously reported the $^1O_2$ reactions with free base 8-oxoguanine in its protonated form ([8-oxoguanine+H]$^+$, protonated at the N3 position) and deprotonated form ([8-oxoguanine − H]$^-$, deprotonated at N1).[11o] The major findings are: 1) There are three DFT-predicted concerted $^1O_2$-addition pathways for [8-oxoguanine+H]$^+$, leading to the products [4,5-dioxetane+H]$^+$, [2,4-OO-8-oxoguanine+H]$^+$ and [2,5-OO-8-oxoguanine+H]$^+$. Nevertheless, all of the three additions encounter tight activation barriers with the activation energies ranging from 0.25 to 1.03 eV above the reactants. Consequently, no O$_2$-adduct was observed for [8-oxoguanine+H]$^+$, both in the absence and the presence of water ligand(s); 2) in contrast to [8-oxoguanine+H]$^+$, a synchronous addition is not feasible for [8-oxoguanine − H]$^-$. Instead, $^1O_2$ may be added to [8-

oxoguanine − H]$^-$ stepwise starting with the formation of [5-OO-8-oxoguanine − H]$^-$, followed by evolution to [4,5-OO–dioxetane − H]$^-$ and [5-OOH^7-8-oxoguanine − H]$^-$. As a result, a mixture of [5-OO-8-oxoguanine − H]$^-$, [4,5-dioxetane − H]$^-$ (major) and [5-OOH^7-8-oxoguanine − H]$^-$ was captured in the products; 3) the oxidation of [8-oxoguanine − H]$^-$ is significant only at low collision energies. The reaction efficiency is 4% at 0.1 eV, higher than those of deprotonated guanine and 9-methylguanine by a factor of 1.6 and 2.2, respectively.[56] The product cross section decreases with increasing E_{col}, becoming negligible above 0.3 eV. This is consistent with the thermodynamics of an exothermic reaction with no barriers above the reactants.

The above comparison has demonstrated the dichotomies between the $^1O_2$ oxidizability of the radical cation of 8-oxoguanine vs. the non-reactivity of the protonated 8-oxoguanine, and between the 5-OO-peroxide product of the radical cation reactant vs. the 4,5-dioxetane product of the deprotonated reactant. All of these have strengthened a premise we demonstrated before,[11o,28h,56–57] that is different ionization states of nucleobase and nucleosides lead to different oxidation mechanisms and products with $^1O_2$.

Conclusion

Gas-phase ion-beam scattering mass spectrometric study has provided a unique tool for investigating the reactions of $^1O_2$ with 9MOG$^{\bullet+}$ and OG$^{\bullet+}$. Both reaction systems have produced barrierless, exothermic products. Direct dynamics simulations and quantum chemistry study were performed for the reaction of 9MOG$^{\bullet+}$ with $^1O_2$ at various single- and multi-reference levels of theory, of which CASPT2 served as a benchmark method to
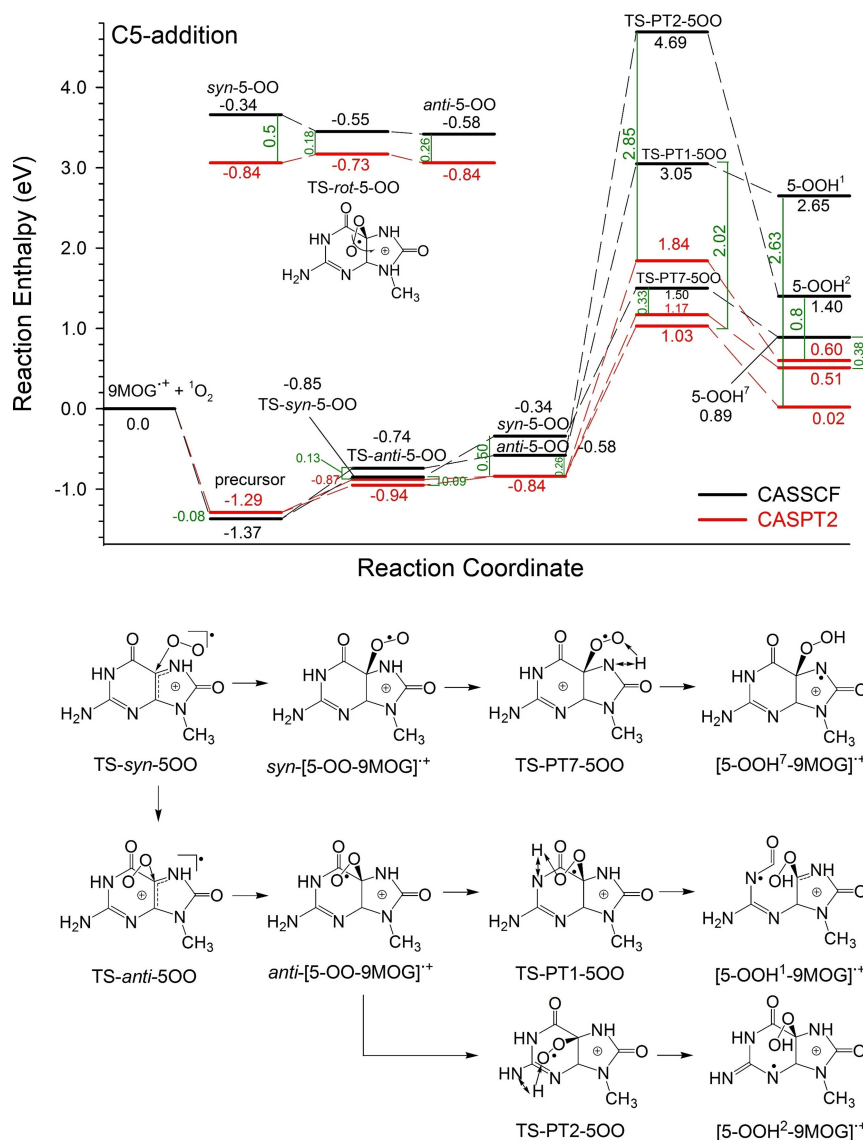
ChemPlusChem

Full Papers
doi.org/10.1002/cplu.202100238

**Chemistry
Europe**
European Chemical
Societies Publishing

Figure 5. Comparison of the PESs for the C5-addition of $^1O_2$ to 9MG$^{•+}$ calculated at CASSCF(21,15)/6-31+G(d,p) and CASPT2(21,15)/6-31G(d,p), using the ωB97XD/6-31+G(d,p)-optimized geometries. Reaction enthalpies were calculated at 298 K including thermal corrections. Reaction structures and rearrangements in TSs are shown in the ChemDraw scheme.

provide the best description of the multiconfigurational PES arising from the mixed open- and closed-shell $^1O_2$ and the open-shell $^1O_2$-adducts and transition states. Guided by E_{col} dependence of reaction cross sections, static reaction PES and molecular dynamics trajectories, the C5-peroxide represents the thermodynamically most feasible and kinetically most favorable product channel for the $^1O_2$ oxidation of 9MOG$^{•+}$ and OG$^{•+}$. This pathway opens at thermal energies and thus is biologically significant. The fact that 9MOG$^{•+}$ and OG$^{•+}$ have higher reaction efficiencies with $^1O_2$ than the 9-methylguanine and 2′-deoxyguanosine radical cations has restated that the OG nucleobase and nucleoside are more vulnerable to oxidative damage than their undamaged parent molecules, not only in neutral molecules but also in their ionized states. The distinctively different $^1O_2$ reaction pathways and products of OG$^{•+}$ than those of protonated and deprotonated 8-oxogua-

nine ions have provided another illustration of the dependence of nucleobase and nucleoside oxidation on their ionization states.

Experimental Section

9MOG was obtained from B. Lippert (University of Dortmund, Germany), which was prepared in W. Pfleiderer laboratory (University of Konstanz, Germany).[58] Other chemicals were purchased from commercial sources. Experimental and computational details are reported in the Supporting Information (including 9MOG$^{•+}$ conformations, reaction energetics and PESs at different levels, and Cartesian coordinates for the calculated structures). Only a brief description is provided below.
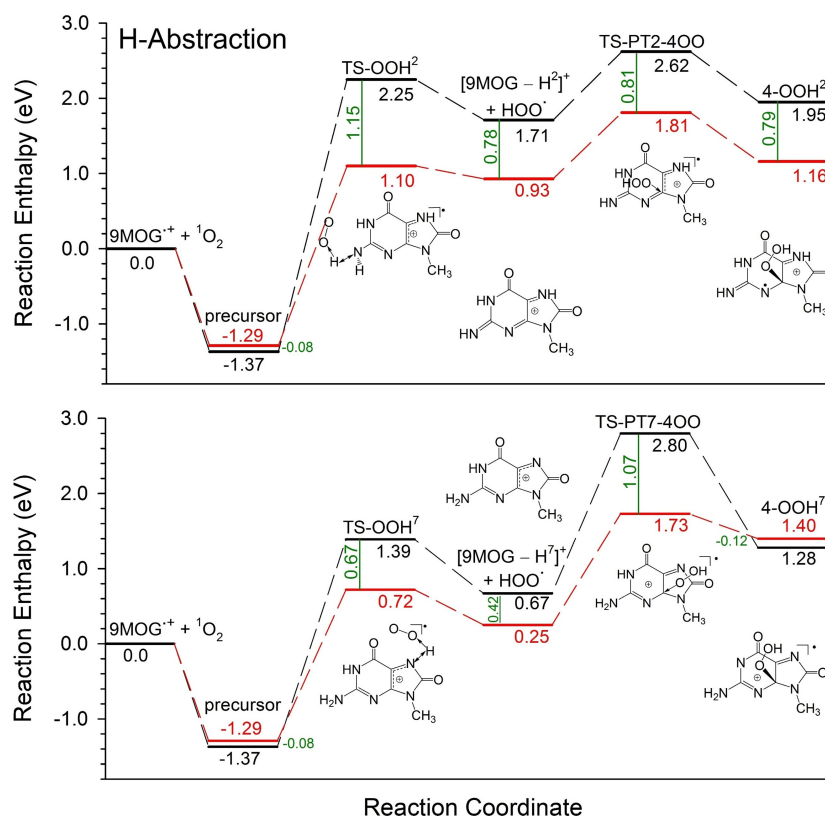
Figure 6. Comparison of the PES for the hydrogen abstraction of 9MG•+ by $^1O_2$ calculated at CASSCF(21,15)/6-31+G(d,p) and CASPT2(21,15)/6-31G(d,p), using the ωB97XD/6-31+G(d,p)-optimized geometries. Reaction enthalpies were calculated at 298 K including thermal corrections. Reaction structures and rearrangements in TSs are shown in the ChemDraw scheme.

Ion-molecule reactions

$^1O_2$ was generated by the reaction of $H_2O_2 + Cl_2 + 2KOH \rightarrow {}^1O_2/{}^3O_2 + 2KCl + 2H_2O$.[59] In brief, Cl_2 was mixed with He and bubbled through the H_2O_2/KOH slush maintained at $-17\,°C$. Cl_2 reacted completely with H_2O_2 and produced a mixture of $^1O_2$, $^3O_2$ and water, and water was removed by passing the gas products through a $-70\,°C$ cold trap. The absolute concentration of $^1O_2$ was determined by measuring the $^1O_2$ phosphorescence ($a^1\Delta_g \rightarrow X^3\Sigma_g^-$) at 1270 nm[60] using a calibrated emission detector.[61] A steady concentration of $^1O_2$ (~15%) was obtained in the experiment.

Reactions of $^1O_2$ with OG•+ and 9MOG•+ were conducted on a home-built ESI guided-ion-beam scattering tandem mass spectrometer.[33,35] A 3:1 methanol/water solution containing 0.25 mM $Cu(NO_3)_2$ and 0.25 mM OG was electrosprayed into the air. The Cu(II)—OG complexes formed in ESI were introduced into the source chamber of the mass spectrometer through a heated capillary. A skimmer was located 3 mm away from the end of the capillary, separating the source chamber and a hexapole ion guide. An electrical field applied between the capillary and the skimmer prompted CID of Cu^{II}—OG complexes with the background gas in the chamber, of which the dissociation of $[Cu^{II}(OG)_3]^{•2+}$ produced $[Cu^I(OG)_2]^+ + OG^{•+}$. We found that the intensity of OG•+ was increased by adding equimolar concentration of 2′-deoxyguanosine in the ESI solution, i.e., 7×10^4 counts/sec (cps) of OG•+ in the presence of 0.25 mM 2′-deoxyguanosine vs. 3×10^4 cps in the absence of the co-ligand. Likewise, 9MOG•+ was generated using an ESI solution of an equimolar concentration mixture of 9MOG, 2′-deoxyguanosine and $Cu(NO_3)_2$ with an ion beam intensity of 10×10^4 cps.

The OG•+ or 9MOG•+ cations were transported into the hexapole ion guide for collisional focusing and thermalization, and then mass selected by a quadrupole mass filter. The mass-selected reactant ions were injected into an octopole ion guide that passes the scattering cell containing the $^1O_2$ gas. In addition to trapping ions in the radial direction, the octopole was biased at a DC potential to adjust the E_{col} between radical cations and $^1O_2$ in the center-of-mass frame. The product ions resulting from ion-molecule reactions and the remaining reactant ions were collected by the octopole, passed into a second quadrupole mass filter for analysis. Reaction cross sections were calculated from the ratio of reactant/product ion intensities, the $^1O_2$ pressure in the scattering cell and the effective cell length. A control experiment was conducted using $^3O_2$ as the collisional gas and confirmed that OG•+ and 9MOG•+ are not reactive with $^3O_2$.

Molecular dynamics simulations and reaction PES calculations

The initial conditions for the collision trajectories of 9MOG•+ with $^1O_2$, including reactant vibrational energy (E_{vib}, including ZPE), rotational energy (E_{rot}), E_{col}, and center-of-mass separation between randomly oriented reactants, were set up using Venus.[43] The purpose of trajectory simulations was to identify reaction pathway (s) and product structure(s). Therefore trajectories were modeling head-on collisions with the impact parameter equal to zero. Hessian-based predictor-corrector algorithm[42f] implemented in Gaussian 09[44] was used to integrate classical equations of motion, with Hessian recalculated every 5 steps. The ωB97XD/6-31G(d) method was chosen for trajectory calculations. ωB97XD over-estimated the $^1O_2$ excitation energy by 0.7 eV and consequently

lowered most of the reaction energies. As such, the trajectories were likely not to miss important reaction. Trajectories were propagated with a step size of 0.25 amu$^{1/2}$Bohr, and terminated when product separation has exceeded 8.0 Å or the trajectory time has reached 3 psec. gOpenMol[62] was used for trajectory visualization. Trajectory outcomes were analyzed using custom programs written for these purposes. A small batch of trajectories were recalculated using the 6-31+G(d,p) basis set, which produced the same collision dynamics and similar product energy distributions as those of ωB97XD/6-31G(d).

Static structures of reaction intermediates, TSs and products were optimized at the ωB97XD/6-31G+(d,p) level of theory. Energies of the DFT optimized structures were refined using CASSCF/6-31+G(d,p)[49b,63] and CASPT2/6-31G(d,p).[51] Reaction enthalpy reported at each level of theory is based on the sum of the electronic energy calculated at the specified level and the 298 K thermal correction at ωB97XD/6-31+G(d,p) (including ZPE which was scaled by factor of 0.975[64]). ωB97XD and CASSCF calculations were completed using Gaussian 09.[44] DLPNO-CCSD(T) calculations and T1 diagnostic were calculated with ORCA 4.[65] CASPT2(21,15) calculations were carried out using MOLCAS 8,[66] for which the shift parameter for ionization potential-electron affinity was set to 0.25 a.u.[67]

Acknowledgements

Conflict of Interest

The authors declare no conflict of interest.

Keywords: ion-molecule reaction · mass spectrometry · nucleosides · reaction mechanisms · singlet oxygen

[1] J. Cadet, P. D. Mascio, in *Modified nucleosides: In biochemistry, biotechnology and medicine* (Ed.: P. Herdewijn), Wiley-VCH Verlag Gmbh & Co. KGaA, Weinheim, **2008**, pp. 29–47.

[2] a) H. Sies, *Oxidative Stress*, Academic Press, **1985**; b) S. Boiteux, J. P. Radicella, *Biochimie* **1999**, *81*, 59–67.

[3] a) D. C. Malins, N. L. Polissar, G. K. Ostrander, M. A. Vinson, *Proc. Natl. Acad. Sci. USA* **2000**, *97*, 12442–12445; b) V. Duarte, J. G. Muller, C. J. Burrows, *Nucleic Acids Res.* **1999**, *27*, 496–502.

[4] S. D. Bruner, D. P. G. Norman, G. L. Verdine, *Nature* **2000**, *403*, 859–866.

[5] a) R. P. Hickerson, C. L. Chepanoske, S. D. Williams, S. S. David, C. J. Burrows, *J. Am. Chem. Soc.* **1999**, *121*, 9901–9902; b) X. Xu, J. G. Muller, Y. Ye, C. J. Burrows, *J. Am. Chem. Soc.* **2008**, *130*, 703–709.

[6] M. A. Lovell, W. R. Markesbery, *Arch. Neurol.* **2001**, *58*, 392–396.

[7] J. Zhang, G. Perry, M. A. Smith, D. Robertson, S. J. Olson, D. G. Graham, T. J. Montine, *Am. J. Pathol.* **1999**, *154*, 1423–1429.

[8] G. Palumbo, *Expert Opin. Drug Delivery* **2007**, *4*, 131–148.

[9] a) P. R. Ogilby, *Chem. Soc. Rev.* **2010**, *39*, 3181–3209; b) S. Nonell, C. Flors, Singlet Oxygen: Applications in Biosciences and Neurosciences, Vol. 1, RSC, Cambridge, **2016**, p. 472 pp; c) P. Di Mascio, G. R. Martinez, S. Miyamoto, G. E. Ronsein, M. H. G. Medeiros, J. Cadet, *Chem. Rev.* **2019**, *119*, 2043–2086.

[10] J. Cadet, J.-L. Ravanat, G. R. Martinez, M. H. G. Medeiros, P. Di Mascio, *Photochem. Photobiol.* **2006**, *82*, 1219–1225.

[11] a) C. Sheu, C. S. Foote, *J. Am. Chem. Soc.* **1995**, *117*, 474–477; b) G. W. Buchko, J. R. Wagner, J. Cadet, S. Raoul, M. Weinfeld, *Biochim. Biophys. Acta Gene Struct. Expression* **1995**, *1263*, 17–24; c) S. Raoul, J. Cadet, J.

Am. Chem. Soc. **1996**, *118*, 1892–1898; d) W. Adam, C. R. Saha-Moeller, A. Schoenberger, *J. Am. Chem. Soc.* **1996**, *118*, 9233–9238; e) R. P. Hickerson, F. Prat, J. G. Muller, C. S. Foote, C. J. Burrows, *J. Am. Chem. Soc.* **1999**, *121*, 9423–9428; f) V. Duarte, D. Gasparutto, L. F. Yamaguchi, J.-L. Ravanat, G. R. Martinez, M. H. G. Medeiros, P. Di Mascio, Paolo, J. Cadet, *J. Am. Chem. Soc.* **2000**, *122*, 12622–12628; g) V. Duarte, D. Gasparutto, M. Jaquinod, J.-L. Ravanat, J. Cadet, *Chem. Res. Toxicol.* **2001**, *14*, 46–53; h) G. R. Martinez, M. H. G. Medeiros, J.-L. Ravanat, J. Cadet, P. Di Mascio, *Biol. Chem.* **2002**, *383*, 607–617; i) J. Cadet, T. Douki, D. Gasparutto, J.-L. Ravanat, *Mutat. Res.* **2003**, *531*, 5–23; j) J. E. B. McCallum, C. Y. Kuniyoshi, C. S. Foote, *J. Am. Chem. Soc.* **2004**, *126*, 16777–16782; k) J.-L. Ravanat, G. R. Martinez, M. H. G. Medeiros, P. Di Mascio, J. Cadet, *Arch. Biochem. Biophys.* **2004**, *423*, 23–30; l) B. Matter, D. Malejka-Giganti, A. S. Csallany, N. Tretyakova, *Nucleic Acids Res.* **2006**, *34*, 5449–5460; m) G. R. Martinez, J.-L. Ravanat, J. Cadet, M. H. Gennari de Medeiros, P. Di Mascio, *J. Mass Spectrom.* **2007**, *42*, 1326–1332; n) B. H. Munk, C. J. Burrows, H. B. Schlegel, *J. Am. Chem. Soc.* **2008**, *130*, 5245–5256; o) Y. Sun, W. Lu, J. Liu, *J. Phys. Chem. B* **2017**, *121*, 956–966; p) A. M. Fleming, C. J. Burrows, *Org. Biomol. Chem.* **2017**, *15*, 8341–8353; q) A. M. Fleming, C. J. Burrows, *DNA Repair* **2017**, *56*, 75–83.

[12] a) P. T. Henderson, J. C. Delaney, J. G. Muller, W. L. Neeley, S. R. Tannenbaum, C. J. Burrows, J. M. Essigmann, *Biochemistry* **2003**, *42*, 9257–9262; b) W. A. Beard, V. K. Batra, S. H. Wilson, *Mutat. Res.* **2010**, *703*, 18–23.

[13] a) W. M. Luo, J. G. E. M. Rachlin, C. J. Burrows, *Org. Lett.* **2000**, *2*, 613–616; b) Y. Ye, J. G. Muller, W. Luo, C. L. Mayne, A. J. Shallop, R. A. Jones, C. J. Burrows, *J. Am. Chem. Soc.* **2003**, *125*, 13926–13927.

[14] H. Yanagawa, Y. Ogawa, M. Ueno, *J. Biol. Chem.* **1992**, *267*, 13320–13326.

[15] S. Steenken, S. V. Jovanovic, *J. Am. Chem. Soc.* **1997**, *119*, 617–618.

[16] F. Prat, K. N. Houk, C. S. Foote, *J. Am. Chem. Soc.* **1998**, *120*, 845–846.

[17] J. Zhou, O. Kostko, C. Nicolas, X. Tang, L. Belau, M. S. de Vries, M. Ahmed, *J. Phys. Chem. A* **2009**, *113*, 4829–4832.

[18] M. Schwell, M. Hochlaf, *Top. Curr. Chem.* **2015**, *355*, 155–208.

[19] a) D. Ly, L. Sanii, G. B. Schuster, *J. Am. Chem. Soc.* **1999**, *121*, 9400–9410; b) Z. A. Doddridge, P. M. Cullis, G. D. D. Jones, M. E. Malone, *J. Am. Chem. Soc.* **1998**, *120*, 10998–10999; c) V. Shafirovich, J. Cadet, D. Gasparutto, A. Dourandin, W. Huang, N. E. Geacintov, *J. Phys. Chem. B* **2001**, *105*, 586–592; d) L. I. Shukla, A. Adhikary, R. Pazdro, D. Becker, M. D. Sevilla, *Nucleic Acids Res.* **2004**, *32*, 6565–6574.

[20] P. Diamantis, I. Tavernelli, U. Rothlisberger, *J. Chem. Theory Comput.* **2020**, *16*, 6690–6701.

[21] a) A. Colasanti, A. Kisslinger, M. Quarto, P. Riccio, *Acta Biochim. Pol.* **2004**, *51*, 1039–1046; b) I. Postiglione, A. Chiaviello, G. Palumbo, *Cancers* **2011**, *3*, 2597–2629; c) V. C. K. Lo, M. K. Akens, S. Moore, A. J. M. Yee, B. C. Wilson, C. M. Whyne, *Breast Cancer Res. Treat.* **2012**, *135*, 391–401.

[22] S. J. Culp, B. P. Cho, F. F. Kadlubar, F. E. Evans, *Chem. Res. Toxicol.* **1989**, *2*, 416–422.

[23] S. Steenken, S. V. Jovanovic, M. Bietti, K. Bernhard, *J. Am. Chem. Soc.* **2000**, *122*, 2373–2374.

[24] J. Reynisson, S. Steenken, *J. Mol. Struct.: Theochem* **2005**, *723*, 29–36.

[25] Y. Sun, M. M. Moe, J. Liu, *Phys. Chem. Chem. Phys.* **2020**, *20*, 14875–14888.

[26] J. Shao, N. E. Geacintov, V. Shafirovich, *Chem. Res. Toxicol.* **2010**, *23*, 933–938.

[27] a) J. Cadet, M. Berger, G. W. Buchko, P. C. Joshi, S. Raoul, J.-L. Ravanat, *J. Am. Chem. Soc.* **1994**, *116*, 7403–7404; b) J. Cadet, T. Douki, J.-L. Ravanat, *Acc. Chem. Res.* **2008**, *41*, 1075–1083; c) W. L. Neeley, J. M. Essigmann, *Chem. Res. Toxicol.* **2006**, *19*, 491–505; d) A. M. Fleming, C. J. Burrows, *Free Radical Biol. Med.* **2017**, *107*, 35–52.

[28] a) S. Wee, R. A. J. O'Hair, W. D. McFadyen, *Rapid Commun. Mass Spectrom.* **2005**, *19*, 1797–1805; b) A. K. Y. Lam, B. F. Abrahams, M. J. Grannas, W. D. McFadyen, R. A. J. O'Hair, *Dalton Trans.* **2006**, issue 42, 5051–5061; c) P. Cheng, D. K. Bohme, *J. Phys. Chem. B* **2007**, *111*, 11075–11082; d) L. Feketeová, G. N. Khairallah, B. Chan, V. Steinmetz, P. Maître, L. Radom, R. A. J. O'Hair, *Chem. Commun.* **2013**, *49*, 7343–7345; e) S. R. Huang, F. Turecek, *J. Phys. Chem. A* **2020**, *124*, 7101–7112; f) S. R. Huang, A. Dang, F. Turecek, *J. Am. Soc. Mass Spectrom.* **2020**, *31*, 1271–1281; g) S. R. Huang, F. Turecek, *J. Am. Soc. Mass Spectrom.* **2021**, *32*, 373–386; h) Y. Sun, M. Tsai, M. M. Moe, J. Liu, *J. Phys. Chem. A* **2021**, *125*, 1564–1576.

[29] J. M. Rice, G. O. Dudek, *J. Am. Chem. Soc.* **1967**, *89*, 2719–2725.

[30] A. Liguori, A. Napoli, G. Sindona, *J. Am. Soc. Mass Spectrom.* **2001**, *12*, 176–179.

[31] I. K. Chu, C. F. Rodriquez, T.-C. Lau, A. C. Hopkinson, K. W. M. Siu, *J. Phys. Chem. B* **2000**, *104*, 3393–3397.

[32] L. Feketeová, E. Yuriev, J. D. Orbell, G. N. Khairallah, R. A. J. O'Hair, *Int. J. Mass Spectrom.* **2011**, *304*, 74–82.

[33] Y. Sun, W. Zhou, M. M. Moe, J. Liu, *Phys. Chem. Chem. Phys.* **2018**, *20*, 27510–27522.

[34] a) D. Venkateswarlu, J. Leszczynski, *J. Comput.-Aided Mol. Des.* **1998**, *12*, 373–382; b) P. Cysewski, *J. Chem. Soc. Faraday Trans.* **1998**, *94*, 3117–3125; c) J. Gu, J. Leszczynski, *J. Phys. Chem. A* **1999**, *103*, 577–584; d) Y. H. Jang, W. A. Goddard, III, K. T. Noyes, L. C. Sowers, S. Hwang, D. S. Chung, *Chem. Res. Toxicol.* **2002**, *15*, 1023–1035; e) V. Verdolino, R. Cammi, B. H. Munk, H. B. Schlegel, *J. Phys. Chem. B* **2008**, *112*, 16860–16873; f) K. M. Uddin, R. A. Poirier, *J. Phys. Chem. B* **2011**, *115*, 9151–9159; g) Z. Lu, A. A. Beckstead, B. Kohler, S. Matsika, *J. Phys. Chem. B* **2015**, *119*, 8293–8301.

[35] Y. Fang, J. Liu, *J. Phys. Chem. A* **2009**, *113*, 11250–11261.

[36] J. Troe, *Chem. Phys. Lett.* **1985**, *122*, 425–430.

[37] B. H. Munk, C. J. Burrows, H. B. Schlegel, *Chem. Res. Toxicol.* **2007**, *20*, 432–444.

[38] N. R. Jena, P. C. Mishra, *J. Phys. Chem. B* **2005**, *109*, 14205–14218.

[39] J.-D. Chai, M. Head-Gordon, *Phys. Chem. Chem. Phys.* **2008**, *10*, 6615–6620.

[40] A. Kumar, M. D. Sevilla, *J. Phys. Chem. B* **2014**, *118*, 5453–5458.

[41] B. F. Yates, W. J. Bouma, L. Radom, *Tetrahedron* **1986**, *42*, 6225–6234.

[42] a) R. Car, M. Parrinello, *Phys. Rev. Lett.* **1985**, *55*, 2471–2474; b) K. K. Baldridge, M. S. Gordon, R. Steckler, D. G. Truhlar, *J. Phys. Chem.* **1989**, *93*, 5107–5119; c) T. Helgaker, E. Uggerud, H. J. A. Jensen, *Chem. Phys. Lett.* **1990**, *173*, 145–150; d) K. Bolton, W. L. Hase, G. H. Peslherbe, in *Modern Methods for Multidimensional Dynamics Computations in Chemistry* (Ed.: D. L. Thompson), World Scientific, Singapore, **1998**, pp. 143–189; e) W. L. Hase, Advances in Classical Trajectory Methods, Vol. 1. Intramolecular and Nonlinear Dynamics. JAI, Greenwich, Conn., **1992**, p. 399; f) V. Bakken, J. M. Millam, H. B. Schlegel, *J. Chem. Phys.* **1999**, *111*, 8773–8777; g) M. Döntgen, M.-D. Przybylski-Freund, L. C. Kröger, W. A. Kopp, A. E. Ismail, K. Leonhard, *J. Chem. Theory Comput.* **2015**, *11*, 2517–2524; h) E. Martínez-Núñez, *Phys. Chem. Chem. Phys.* **2015**, *17*, 14912–14921; i) S. Pratihar, X. Ma, Z. Homayoon, G. L. Barnes, W. L. Hase, *J. Am. Chem. Soc.* **2017**, *139*, 3570–3590; j) X. Ma, W. L. Hase, *Philos. Trans. R. Soc. London Ser. A* **2017**, *375*, 20160204.

[43] W. L. Hase, K. Bolton, P. de Sainte Claire, R. J. Duchovic, X. Hu, A. Komornicki, G. Li, K. Lim, D. Lu, G. H. Peslherbe, K. Song, K. N. Swamy, S. R. Vande Linde, A. Varandas, H. Wang, R. J. Wolf, Texas Tech University Lubbock, TX, **1999**.

[44] M. J. Frisch, G. W. Trucks, H. B. Schlegel, G. E. Scuseria, M. A. Robb, J. R. Cheeseman, G. Scalmani, V. Barone, B. Mennucci, G. A. Petersson, H. Nakatsuji, M. Caricato, X. Li, H. P. Hratchian, A. F. Izmaylov, J. Bloino, G. Zheng, J. L. Sonnenberg, M. Hada, M. Ehara, K. Toyota, R. Fukuda, J. Hasegawa, M. Ishida, T. Nakajima, Y. Honda, O. Kitao, H. Nakai, T. Vreven, J. J. A. Montgomery, J. E. Peralta, F. Ogliaro, M. Bearpark, J. J. Heyd, E. Brothers, K. N. Kudin, V. N. Staroverov, T. Keith, R. Kobayashi, J. Normand, K. Raghavachari, A. Rendell, J. C. Burant, S. S. Iyengar, J. Tomasi, M. Cossi, N. Rega, J. M. Millam, M. Klene, J. E. Knox, J. B. Cross, V. Bakken, C. Adamo, J. Jaramillo, R. Gomperts, R. E. Stratmann, O. Yazyev, A. J. Austin, R. Cammi, C. Pomelli, J. W. Ochterski, R. L. Martin, K. Morokuma, V. G. Zakrzewski, G. A. Voth, P. Salvador, J. J. Dannenberg, S. Dapprich, A. D. Daniels, O. Farkas, J. B. Foresman, J. V. Ortiz, J. Cioslowski, D. J. Fox, Gaussian, Inc, Wallingford, CT, **2013**.

[45] D. G. Liakos, M. Sparta, M. K. Kesharwani, J. M. L. Martin, F. Neese, *J. Chem. Theory Comput.* **2015**, *11*, 1525–1539.

[46] A. Maranzana, G. Ghigo, G. Tonachini, *J. Am. Chem. Soc.* **2000**, *122*, 1414–1423.

[47] a) T. J. Lee, P. R. Taylor, *Int. J. Quantum Chem. Quantum Chem. Symp.* **1989**, *36*, 199–207; b) D. Jayatilaka, T. J. Lee, *J. Chem. Phys.* **1993**, *98*, 9734–9747.

[48] a) J. C. Rienstra-Kiracofe, W. D. Allen, H. F. Schaefer, III, *J. Phys. Chem. A* **2000**, *104*, 9823–9840; b) T. J. Lee, *Chem. Phys. Lett.* **2003**, *372*, 362–367.

[49] a) B. O. Roos, P. R. Taylor, E. M. Siegbahn, *Chem. Phys.* **1980**, *48*, 157–173; b) J. Olsen, B. O. Roos, P. Jørgensen, H. J. A. Jensen, *J. Chem. Phys.* **1988**, *89*, 2185–2192.

[50] B. Thapa, B. H. Munk, C. J. Burrows, H. B. Schlegel, *Chem. Eur. J.* **2017**, *23*, 5804–5813.

[51] a) K. Andersson, P. A. Malmqvist, B. O. Roos, *J. Chem. Phys.* **1992**, *96*, 1218–1226; b) M. Abe, G. Gopakmar, T. Nakajima, K. Hirao, in *Radiation Induced Molecular Phenomena in Nucleic Acids* (Eds.: K. Shukla, M. K., J. Leszczynski), Springer, Netherlands, **2008**, pp. 157–177.

[52] R. J. Buenker, S. D. Peyerimhoff, *Theor. Chim. Acta* **1974**, *35*, 33–58.

[53] F. Sevin, M. L. McKee, *J. Am. Chem. Soc.* **2001**, *123*, 4591–4600.

[54] B. Marchetti, T. N. V. Karsili, *Chem. Commun.* **2016**, *52*, 10996–10999.

[55] a) F. Weigend, M. Haser, H. Patzelt, R. Ahlrichs, *Chem. Phys. Lett.* **1998**, *294*, 143–152; b) P. Jurecka, P. Nachtigall, P. Hobza, *Phys. Chem. Chem. Phys.* **2001**, *3*, 4578–4582.

[56] a) W. Lu, J. Liu, *Chem. Eur. J.* **2016**, *22*, 3127–3138; b) W. Lu, H. Teng, J. Liu, *Phys. Chem. Chem. Phys.* **2016**, *18*, 15223–15234.

[57] W. Lu, Y. Sun, W. Zhou, J. Liu, *J. Phys. Chem. B* **2018**, *122*, 40–53.

[58] R. K. O. Sigel, E. Freisinger, B. Lippert, *JBIC J. Biol. Inorg. Chem.* **2000**, *5*, 287–299.

[59] a) A. Midey, I. Dotan, A. A. Viggiano, *J. Phys. Chem. A* **2008**, *112*, 3040–3045; b) Y. Fang, F. Liu, A. Bennett, S. Ara, J. Liu, *J. Phys. Chem. B* **2011**, *115*, 2671–2682.

[60] W. J. Lafferty, A. M. Solodov, C. L. Lugez, G. T. Fraser, *Appl. Opt.* **1998**, *37*, 2264–2270.

[61] F. Liu, Y. Fang, Y. Chen, J. Liu, *J. Phys. Chem. B* **2012**, *116*, 6369–6379.

[62] L. Laaksonen, *Vol. 3.0*, 3.0 ed., Center for Scientific Computing, Espoo, Finland, **2005**, p. available at www.csc.fi/gopenmol/.

[63] B. O. Roos, P. R. Taylor, P. E. M. Sigbahn, *Chem. Phys.* **1980**, *48*, 157–173.

[64] I. M. Alecu, J. Zheng, Y. Zhao, D. G. Truhlar, *J. Chem. Theory Comput.* **2010**, *6*, 2872–2887.

[65] F. Neese, *WIREs Comput. Mol. Sci.* **2018**, *8*, e1327.

[66] F. Aquilante, J. Autschbach, R. K. Carlson, L. F. Chibotaru, M. G. Delcey, L. De Vico, I. F. dez. Galvan, N. Ferre, L. M. Frutos, L. Gagliardi, M. Garavelli, A. Giussani, C. E. Hoyer, G. Li Manni, H. Lischka, D. Ma, P. Å. Malmqvist, T. Mueller, A. Nenov, M. Olivucci, T. B. Pedersen, D. Peng, F. Plasser, B. Pritchard, M. Reiher, I. Rivalta, I. Schapiro, J. Segarra-Marti, M. Stenrup, D. G. Truhlar, L. Ungur, A. Valentini, S. Vancoillie, V. Veryazov, V. P. Vysotskiy, O. Weingart, F. Zapata, R. Lindh, *J. Comput. Chem.* **2016**, *37*, 506–541.

[67] a) D. Roca-Sanjuán, M. Rubio, M. Merchán, L. Serrano-Andrés, *J. Chem. Phys.* **2006**, *125*, 084302; b) G. Ghigo, B. O. Roos, P.-A. Malmqvist, *Chem. Phys. Lett.* **2004**, *396*, 142–149.